



Photonic crystal optical parametric oscillator

Gabriel Marty^{1,2}, Sylvain Combri ¹, Fabrice Raineri^{2,3} and Alfredo De Rossi¹✉

We report a new class of optical parametric oscillators, based on a 20- m-long semiconductor photonic crystal cavity and operating at telecom wavelengths. Because the confinement results from Bragg scattering, the optical cavity contains a few modes, approximately equispaced in frequency. Parametric oscillation is reached when these high-quality-factor modes are thermally tuned into a triply resonant configuration, whereas any other parametric interaction is strongly suppressed. The lowest pump power threshold is estimated to be 50–70  W. This source behaves as an ideal degenerate optical parametric oscillator, addressing the needs in the field of quantum optical circuits and paving the way towards the dense integration of highly efficient nonlinear sources of squeezed light or entangled photons pairs.

Miniaturization of devices has been a primary objective in microelectronics and photonics for decades, aimed at denser integration, enhanced functionalities and drastic reduction of power consumption. Headway in nanophotonics is currently linked to the progress in concepts and technologies necessary for applications in information and communication¹, brain-inspired computing², medicine and sensing³, and quantum information⁴. Among all nanostructures, semiconductor photonic crystals (PhCs)⁵ occupy a prominent position as they enable the fabrication of quasi-ultimate optical cavities⁶. Low-threshold laser diodes^{7,8} or Raman lasers⁹, low-power-consuming optical memories¹⁰, efficient single-photon sources¹¹ or single-photon quantum gates¹² are impressive examples of their capabilities. The PhC implementation of an important class of optical sources, namely optical parametric oscillators (OPOs), is missing.

An OPO emits coherent light relying on the ultrafast nonlinear response of matter for the stimulated emission of photon pairs. OPOs can generate light within a spectral range limited by only the transparency of the nonlinear material. As the generated photons are correlated, OPOs are also sources of non-classical light for quantum optics^{13,14} and quantum computing¹⁵. OPOs were originally available only as solid-state optical devices, tending to be bulky and expensive. About 15 years ago, the progress in the fabrication of resonators with high quality factor (*Q*) resonators led to microcavity OPOs^{16,17} and the ensuing birth of a new domain in nonlinear photonics. They have been constantly improved in virtually all respects and have been recently integrated with laser diodes into very compact packages^{18,19}.

Microresonators are based on disks or rings, where the confinement results from the total internal reflection. Essential here is engineering the dispersion of the propagating waves, to control the nonlinear interaction of a large number of modes. This enables soliton combs²⁰ or the ultrabroadband generation of light^{21–23}, to give a few examples.

In contrast, PhC cavities are fundamentally different devices that confine a small number of modes within a photonic bandgap^{24,25}. Moreover, high-*Q* resonances with diffraction-limited mode volumes of about $(\lambda/n)^3$, with λ the wavelength and n the refractive index, are possible in a PhC cavity^{5,6}, which would lead to a favourable figure of merit Q^2/V , with V the volume occupied by the mode, for lowering the power threshold for parametric interactions²⁶. The possibility of a PhC OPO was considered theoretically more than a

decade ago^{27,28} and experimental attempts to achieve efficient parametric interaction have been made^{29,30}; however, demonstration of OPOs has been extremely challenging.

PhC OPO technology

Our PhC OPOs harness triply resonant degenerate four-wave mixing (FWM) (Fig. 1a). For this Kerr optical nonlinear process, energy conservation dictates the relation between the pump and the generated photons ($2\omega_p = \omega_i + \omega_s$), meaning that the new angular frequencies for the idler (ω_i) and signal (ω_s) are generated symmetrically with respect to the pump frequency ω_p . Thus, resonant enhancement is only possible if three cavity eigenfrequencies ($\omega_0, \omega_+, \omega_-$) are rigorously equispaced. This condition is in general not satisfied in PhC resonators. Triply resonant parametric interaction was observed in a system made of three coupled PhC nanocavities, but with a limited efficiency due to a low *Q*-factor²⁹ or not well-controlled frequency spacing³⁰. In fact, the control of the frequency spacing is ultimately limited by structural disorder: even in state-of-the-art PhC technology, resonances deviate from their design value by about 40 GHz (ref. 31). For this reason, in absence of a tuning mechanism, the eigenmode linewidth must be large enough to allow triply resonant FWM. This corresponds to $Q < 5 \times 10^3$, clearly hindering the opportunity offered by PhCs⁶.

In this Article, we demonstrate a PhC OPO operated at ultralow power. This result was achieved owing to three key features: first, we designed the cavity to have equispaced eigenfrequencies, then, we introduced a differential thermo-refractive tuning mechanism to compensate for the residual spectral misalignment caused by fabrication imperfections, and, finally, we used the III–V semiconductor $\text{In}_{0.5}\text{Ga}_{0.5}\text{P}$ as the constitutive material of our cavity. The large electronic bandgap of this material enables the mitigation of two-photon absorption³², which otherwise clamps nonlinear conversion efficiency below parametric oscillations.

The PhC cavity³³ is designed to create an effective parabolic potential for the optical field (Fig. 1b) such that eigenfrequencies are equispaced and the eigenmodes correspond to Gauss–Hermite functions. The design (Fig. 1c) consists of a suspended membrane with a regular hexagonal lattice of holes with period a , except for a line of missing holes, where light can propagate. There, we introduce a bichromatic lattice³⁴, by modifying the period a' of the innermost row of holes. The localization of the field and the free spectral range (FSR) between higher-order modes are controlled

¹Thales Research and Technology, Campus Polytechnique, Palaiseau, France. ²Centre de Nanosciences et de Nanotechnologies, CNRS, Universit  Paris Saclay, Palaiseau, France. ³Universit  Paris Diderot, Paris, France. ✉e-mail: alfredo.derossi@thalesgroup.com

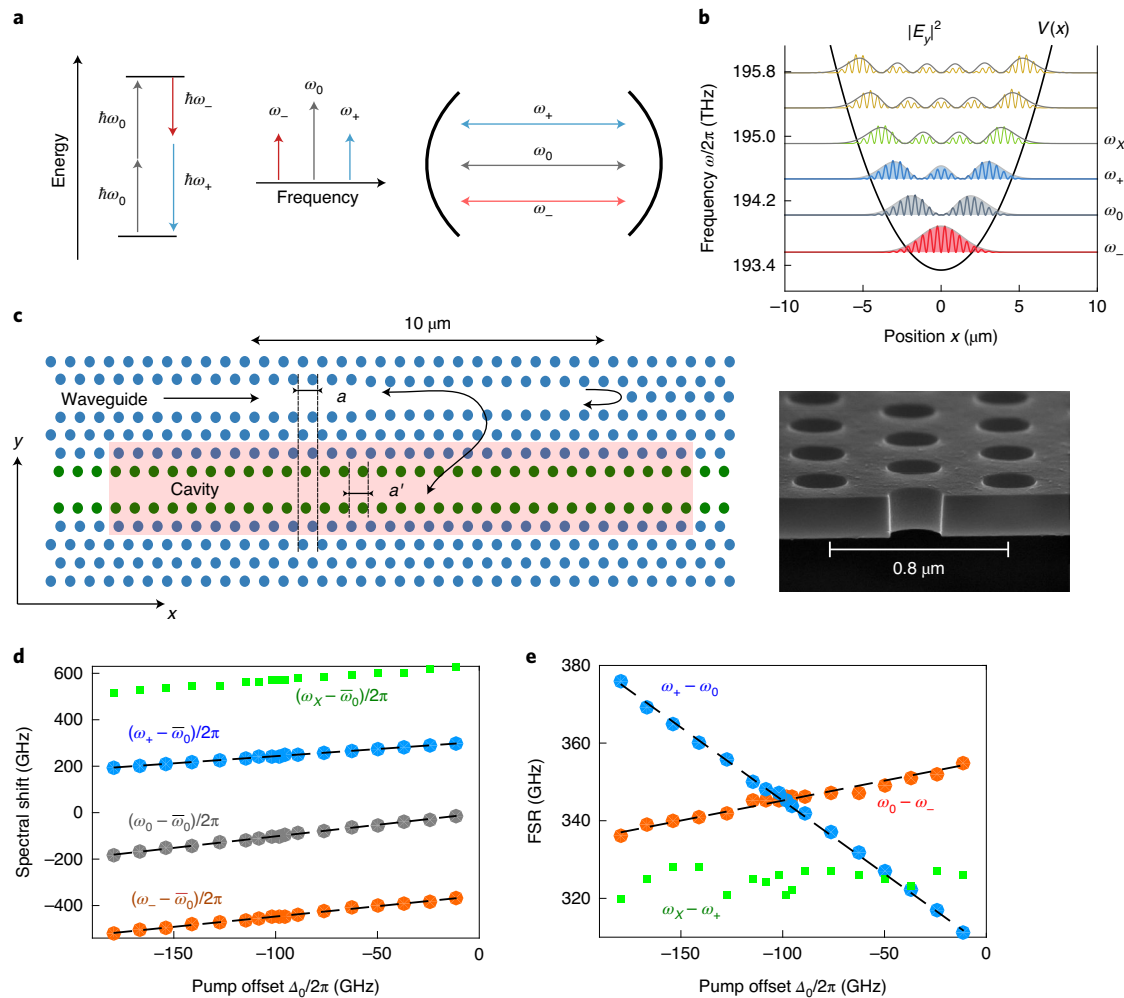


Fig. 1 | Triply resonant PhC cavity. **a**, Concept of the triply resonant degenerate OPO where resonant modes respect the energy conservation $2\hbar\omega_0 = \hbar\omega_+ + \hbar\omega_-$, where \hbar is the reduced Planck constant. **b**, Calculated Hermite-Gauss modes corresponding to an effective parabolic potential for photons (grey solid lines) and eigenmode frequencies ω_- , ω_0 , ω_+ and ω_x , and field amplitudes (coloured lines) of the bichromatic PhC cavity. The filled curves denote a triplet of interacting modes. **c**, Device layout with periods a and a' and access waveguide, and scanning electron microscopy image of the InGaP membrane. The curved line with two arrows represent evanescent coupling between the waveguide and the cavity, and the single curved arrow the reflection at the end of the waveguide. **d**, Measured frequencies of the first four modes (relative to cold resonance $\bar{\omega}_0$) as a function of the pump offset Δ_0 and linear fit (dashed lines). **e**, Corresponding eigenfrequency intervals (FSR).

by the commensurability parameter a'/a . Choosing $a'/a = 0.98$ corresponds to an FSR of about 400 GHz and the field envelopes are very close to Gauss-Hermite functions (Fig. 1b). The optical access to the modes is provided by a single-ended waveguide on the side terminated with a mode adapter to maximize coupling to an optical fibre³⁵.

Operation

Our fabrication process ineluctably induces fluctuations on the targeted eigenfrequencies that result in a misalignment (50 GHz on average) far greater than the resonance linewidth, below 1 GHz (details in Supplementary Section II.C). We use thermal tuning to compensate for this deviation. Thermal control of the parametric interaction has been implemented by individually controlling two coupled resonators³⁶ or exploiting the dispersive nature of the thermo-refractive effect²³. In our approach, a localized dissipation induces a spatial gradient in the refractive index of the material. In general, the spatial overlap of each mode with the perturbation of the refractive index will be different, and so will the corresponding spectral shift of the resonances. Local heating can be realized

through the projection on the sample surface of a patterned incoherent pumping beam³⁷, this method being limited by the precision of the projection system. In our work, this effect is automatically achieved when the pump mode '0' is resonantly excited, as the energy dissipated induces a temperature gradient. Importantly, Fig. 1b shows that the Gauss-Hermite modes differ markedly in their spatial energy distribution, such that the effect of the temperature gradient on the differential spectral shift of the modes is enhanced. Details are given in Supplementary Section II.A.

To demonstrate thermal tuning, we have performed a pump-probe measurement of the reflection spectra as the pump laser at ω_p and constant power 0.8 mW is swept from blue to red across the resonance. This is achieved using an optical homodyne technique (Methods) using an additional swept laser to detect with high accuracy the pump and the ω_+ and ω_- modes involved in the FWM process. As shown in Fig. 1d, the pumped mode '0' redshifts from $\bar{\omega}_0$ (cold) to ω_0 (hot) while the other modes shift differently as expected. The misalignment of the hot cavity (corresponding to the dispersion) $2\Delta_x = 2\omega_0 - \omega_- - \omega_+$ is deduced from these measurements and is found to follow $2\Delta_x = 2\bar{\Delta}_x + 0.48\Delta_0$ to the first order,

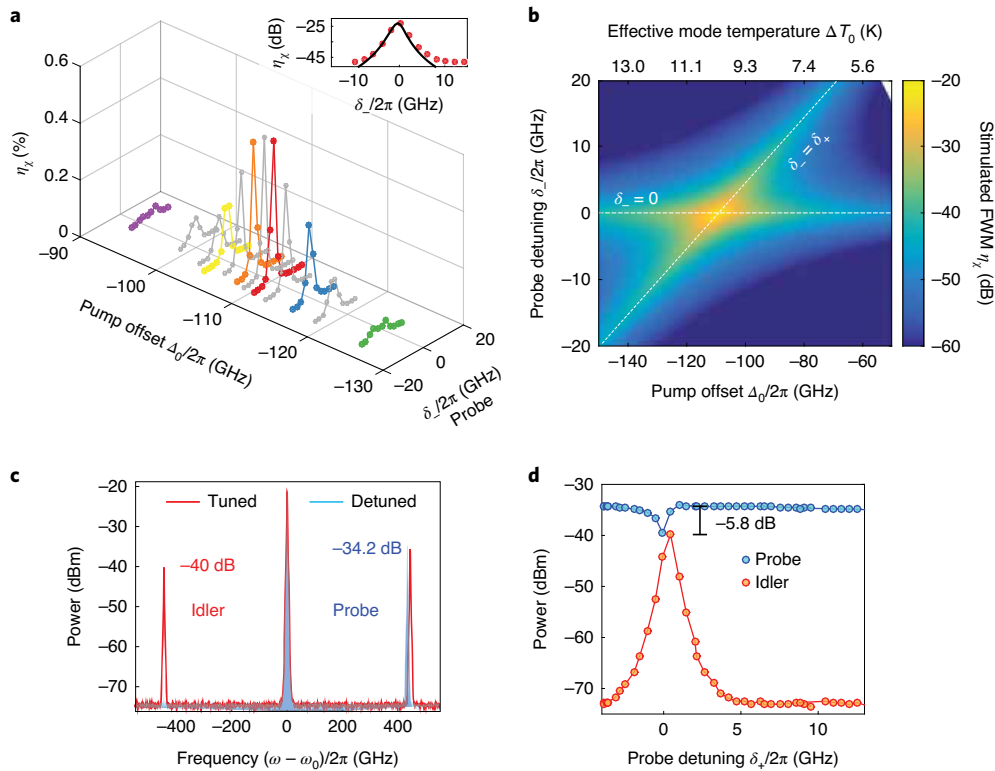


Fig. 2 | Stimulated FWM. **a**, Measured stimulated FWM efficiency η_x as a function of the pump offset Δ_0 and probe detuning δ_- . Inset: comparison with the theory (black line) for the red curve (see Supplementary Fig. 3 for full comparison). The coloured lines and markers represent the different pump offsets. **b**, Calculated false colour map of the efficiency η_x of stimulated FWM as a function of the probe detuning δ_- and pump offset with corresponding effective mode temperature rise ΔT_0 for mode 0. The white lines represent the poles of equation (1). **c**, Stimulated FWM in a resonator with larger Q_{avg} . Raw spectra centred on the pump ω_0 as a function of the probe detuning δ_- spectra for a tuned (red) and detuned (blue) probe. **d**, Reflected probe (blue) and idler (red) power versus probe detuning.

where $\bar{\Delta}_x$ is the misalignment of the ‘cold’ cavity and $\Delta_0 = \omega_p - \bar{\omega}_0$ is the pump offset. This shows that an originally mismatched triplet can eventually be aligned by adjusting the pump frequency, which is clearly observed in Fig. 1e where the two considered FSRs are equalized (crossing of blue and red lines).

We now investigate how this tuning mechanism affects the parametric gain in stimulated FWM measurements, where an additional laser (‘signal’) at ω_s is swept across the resonance at ω_- while the pump frequency is fixed and an idler wave is generated at $\omega_i = 2\omega_p - \omega_s$. As a matter of fact, the stimulated efficiency $\eta_x = P_i/P_s$, defined as the ratio between the output idler power (P_i) over the input signal power (P_s), is directly related to the parametric gain and the loss of the cavity. In fact, parametric oscillation is reached when the gain is large enough to compensate for the loss, and the stimulated efficiency diverges (Supplementary equation 8). The measured values of η_x (details in Supplementary Section II.D) for a sample with an average Q -factor $Q_{\text{avg}} = (Q_0^2 Q_- Q_+)^{1/4}$ of about 7×10^4 are shown in Fig. 2a as a function of the pump offset for an input pump power of 700 μW . The efficiency η_x peaks at 0.4% (−25 dB) when $\Delta_0/2\pi = -110$ GHz, in agreement with the triply resonant configuration predicted by our thermal tuning measurements shown in Fig. 2b. To support these results, an analytical model (Supplementary Section I) is derived and η_x in the limit of undepleted pump and low parametric gain, becomes:

$$\eta_x = \eta_x^{(\text{max})} \mathcal{L}\left(\frac{\delta_0}{\Gamma_0}\right)^2 \mathcal{L}\left(\frac{\delta_-}{\Gamma_-}\right) \mathcal{L}\left(\frac{\delta_+}{\Gamma_+}\right) \quad (1)$$

where $\delta_0 = \omega_p - \omega_0$, $\delta_- = \omega_s - \omega_-$ and $\delta_+ = \omega_i - \omega_+$ are the frequency detunings of the pump, signal and idler with respect to the hot resonances, and Γ_0 , Γ_- and Γ_+ are the photon damping rates in the corresponding modes ($\Gamma = \omega/Q$). $\mathcal{L}(x)$ is the Lorentzian function. The maximum achievable efficiency $\eta_x^{(\text{max})}$ is obtained when the triplet is aligned and when the generated frequencies match the resonant modes ($\delta_0 = \delta_- = \delta_+ = 0$). The calculated map of η_x versus the pump offset and probe detuning δ_- reveals two local peaks merging into an absolute maximum of efficiency, corresponding to a perfectly aligned cavity (Fig. 2b). Remarkably, the measurements are in quantitative agreement with our model, as per the inset of Fig. 2a, when the parameters are either calculated or measured, and the intracavity power adjusted by less than 10% to account for experimental uncertainties (more details in Supplementary Section III.A). The thermal tuning technique allows reaching a larger FWM efficiency as resonators with larger Q -factors can still be tuned to form an equispaced triplet. We performed stimulated FWM on a sample with a larger average $Q = 1.5 \times 10^5$. It results in a drastic improvement of the efficiency that rises up to 26% (−5.8 dB) with an on-chip pump power of 80 μW (Fig. 2c,d). We also note that the dependence of the efficiency on the probe detuning (Fig. 2c) is very sharp, because of the triple resonant enhancement of FWM.

Optical parametric oscillation

In these samples, parametric oscillation is not observed, meaning that the maximum realizable parametric gain is not sufficient to compensate for cavity loss. This value is entirely determined by the cavity optical properties (Q , mode volume, nonlinear cross-section,

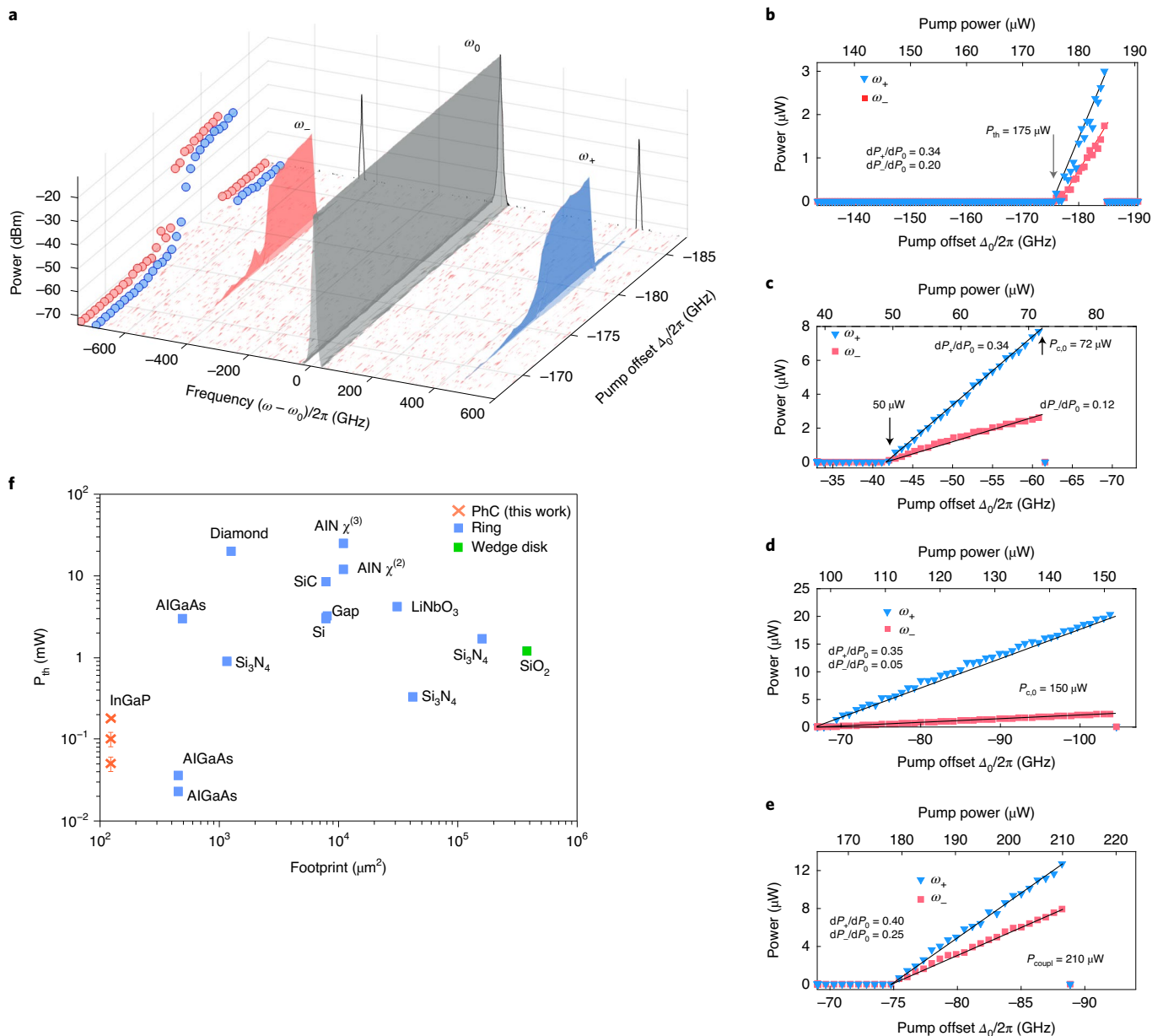


Fig. 3 | Parametric oscillation. **a**, Raw optical spectrum (cavity b8, resolution 4 GHz, centred at the pump frequency) as the pump offset is changed. The threshold is overcome as the intracavity pump energy increases. Markers represent the raw power on the red and blue side and the solid black line is the spectrum at maximum OPO emission. **b–e**, On-chip power in the blue ω_+ and red ω_- (markers) as a function of the pump offset and equivalent pump power in the cavity $P_{\text{c},0}$ with a threshold of 175 μW for cavity b8 (**b**), 50 μW for cavity a5 (**c**), 100 μW for cavity a12 (**d**) and 180 μW for cavity a7. Lines indicate the slope efficiency. **f**, OPO pump threshold as a function of the footprint compared with state the art in microring and racetrack resonators made of different materials (details and references are in Supplementary Table IV).

material nonlinearity) and the pump power level required to align the three modes. Its value is therefore unique for each triplet of modes. Eventually, parametric oscillation is demonstrated for a resonator with $Q_{\text{avg}} \approx 2.5 \times 10^5$. The sample is pumped with an on-chip power level below 200 μW , which is enough to align a triplet of adjacent resonances. As the pump offset $\Delta_0/2\pi < -170$ GHz, the red ω_- and blue ω_+ signals emerge from noise (-73 dBm = 50 pW), as shown in Fig. 3a. When approaching -175 GHz, they abruptly increase by four orders of magnitude, a clear indication of an oscillation threshold. Interestingly, the pump offset, is, to a good approximation, directly proportional to the energy stored in the pump mode as the spectral shift is induced by linear absorption

(Supplementary Section II.A). Therefore, the result can be cast in a more familiar representation by estimating the equivalent pump power circulating in the cavity $P_{\text{c},0}$ in Fig. 3b. Above the threshold $P_{\text{c},0} > P_{\text{th}} = 175 \mu\text{W}$, with $P_{\text{c},0}$ above the threshold power level P_{th} , the on-chip-generated power increases linearly with $\eta_{\pm}(P_{\text{c},0} - P_{\text{th}})/2$, with η_{\pm} the escape efficiency³⁸ from the side modes (defined as $\kappa_{\pm}/\Gamma_{\pm}$; see also Supplementary Tables I and III) and κ the cavity to waveguide coupling rate. More than 50% of the excess pump power is converted. Strikingly, the threshold expected from our model is 170 μW (Supplementary Table III). Experiments have been repeated with three other candidates, labelled a5, a7 and a12, with suitable parameters: $Q_{\text{avg}} > 2 \times 10^5$ and $0 < \Delta_0/2\pi < 50$ GHz. As shown in

Fig. 3c–e, they all demonstrate OPO over a larger operating range, generate more power and have a lower threshold. In particular, the estimate is $P_{\text{th}} = 50\text{--}70\ \mu\text{W}$ for sample a5. The methodology, the reproducibility of the results and the estimate of the uncertainties is broadly discussed in Supplementary Section III.B and it is shown that the results are consistent with the prediction based on the simple equation:

$$P_{\text{th}} = \frac{\epsilon_r V_{\chi} \omega}{8c_0 n_2} \frac{1}{Q_{\text{avg}}^2} \frac{1}{\eta_0} \quad (2)$$

with ϵ_r the relative dielectric permittivity, c_0 the speed of light in vacuum, n_2 the Kerr nonlinear index (Supplementary Table I), the measured Q_{avg} and the cavity coupling efficiency of the pumped mode $\eta_0 = \kappa_0 / I_0$. We also note that the corresponding energy stored in the cavity is below 30 fJ, and even about 10 fJ in the best device (Supplementary Section III.B). The energy at the threshold is set by the loss rate at the side modes, hence to $Q_+ Q_-$. Importantly, if the energy in the cavity is below the level at which nonlinear absorption takes over linear absorption, then a possibly detrimental thermal runaway is avoided, which explains why OPO was observed only at large Q (Supplementary Section II.A and Supplementary Table III).

Discussion

To set this result in the context of integrated OPOs, we consider the power at threshold P_{th} as a function of the device footprint (Fig. 3f). The performance of our ultracompact system based on interacting standing waves is already comparable to that of recently demonstrated microring and racetrack OPOs, which exhibit power thresholds between 30 μW and 25 mW. We note that the resonator footprint here is defined as the smallest area that ensures the confinement of the modes. It corresponds in our case to $20 \times 6\ \mu\text{m}^2$, including the coupling waveguide shown in Fig. 1c. It is apparent that the low power threshold of our PhC OPO results from the strong confinement of the interacting modes and the large nonlinearity of semiconductors, compensating for the moderately large Q -factor, compared with crystalline, silicon nitride or silica resonators. Confinement is an essential point here. Taking into account the spatial overlap between the interaction modes, which corresponds to the phase-matching condition in waveguides, leads to the nonlinear interaction volume (equation (2)), which is here $V_{\chi} = 5.7\ \mu\text{m}^3$. This is about a factor of ten smaller than the corresponding interaction volume deduced for the ring resonator $V_{\chi, \text{ring}} = 1.54 \times 2\pi A_{\text{eff}} R = 50\ \mu\text{m}^3$ (Supplementary Section III.C), with A_{eff} the effective area and R the radius of the ring. The importance of this result is having made a step towards an idealized device with the smallest possible interaction volume. So far, lower power thresholds were observed very recently³⁹ in an AlGaAs-based microring ($\sim 30\ \mu\text{W}$), owing to the larger the nonlinearity of the material and much higher Q -factors. Yet, lower values (down to 5 μW) are reported only in crystalline resonators with an ultrahigh Q -factor and based on the second-order nonlinearity⁴⁰. Considering that current state-of-the-art PhC cavities⁶ exhibit $Q > 10^7$, OPOs with power thresholds approaching the microwatt level can be realistically considered if the Q -factor of our resonators could be improved to be larger than 10^6 . This could be achieved using surface passivation techniques such as in ref. ³⁹, which we have not yet used.

As in any other laser source, power threshold is not the sole figure of merit. The overall energy efficiency transfer from the pump to the side modes is also crucial. In our case, the estimated total (signal + idler) on-chip-generated power is about 20 μW , as shown in Fig. 3d,e, leading to a conversion efficiency that is about 15% of the coupled pump power. This value is comparable to the value of 17% very recently reported in AlN ring resonators⁴¹, which are operated at much larger power (10 mW) and exploit the $\chi^{(2)}$ nonlinearity. Moreover, the measured slope efficiency (signal + idler)

is about 50% in almost all our measurements, limited by only the escape efficiency η_{\pm} (Supplementary Table III). In this respect, an increase of the Q -factor would offer more room for increasing η_{\pm} without sacrificing the power threshold.

Finally, it is interesting to point out that our OPO behaves as a pure degenerate parametric system with only three cavity modes interacting. Simultaneous alignment of more than one triplet is very unlikely. This is apparent in Fig. 1e, where another triplet (x , + and 0) is aligned at a different pump offset $\Delta_0 \approx 50\ \text{GHz}$. While this still allows non-degenerate stimulated FWM, this process is highly inefficient and might be neglected in most cases. Moreover, we show that other modes do not interact at all (Supplementary Section III.B). For the same reason, resonant nonlinear contributions such as Raman can be ignored, unless the resonator is deliberately designed for this, as in ref. ⁹.

It has been recently pointed out that a pure parametric system is highly desirable for some applications. In particular, achieving squeezing on chip using a degenerate OPO has drawn a lot of interest recently^{38,42–44}. Moreover, it has been shown very recently that a network of coupled degenerate OPOs could be implemented on chip to implement a coherent Ising machine⁴⁵. A different idea has also been proposed recently to use a degenerate OPO, as a ‘noise eater’⁴⁶. In a ring resonator, there are strategies to control higher-order interactions, for instance, by inducing side-wall corrugation⁴⁷, adding an auxiliary resonator^{36,38} or implementing narrowband FWM by implementing a special dispersion profile^{21,23}. Here the device operates naturally as a degenerate triply resonant OPO, although it could in principle be possible to achieve efficient cascaded interactions with some additional engineering⁴⁸ and tuning.

In conclusion, we have demonstrated, to the best of our knowledge, the parametric oscillation regime in a PhC cavity. In addition to the low operating pump power (50–70 μW), the efficient conversion to the sidebands (combined slope efficiency $\sim 50\%$) and the absence of competing parametric interactions, this source is amenable to incorporation within sophisticated optical circuits⁴⁹. This demonstration opens up exciting avenues for building an integrated all-semiconductor platform to optically generate and process both classical and quantum data.

Data availability

The data that support the plots within this paper and other findings of this study are available from the corresponding author upon reasonable request.

Online content

Any methods, additional references, Nature Research reporting summaries, source data, extended data, supplementary information, acknowledgements, peer review information; details of author contributions and competing interests; and statements of data and code availability are available at <https://doi.org/10.1038/s41566-020-00737-z>.

Received: 25 March 2020; Accepted: 9 November 2020;

Published online: 21 December 2020

References

1. Sun, C. et al. Single-chip microprocessor that communicates directly using light. *Nature* **528**, 534–538 (2015).
2. Feldmann, J., Youngblood, N., Wright, C., Bhaskaran, H. & Pernice, W. All-optical spiking neurosynaptic networks with self-learning capabilities. *Nature* **569**, 208–214 (2019).
3. Estevez, M. C., Alvarez, M. & Lechuga, L. M. Integrated optical devices for lab-on-a-chip biosensing applications. *Laser Photon. Rev.* **6**, 463–487 (2012).
4. Caspani, L. et al. Integrated sources of photon quantum states based on nonlinear optics. *Light Sci. Appl.* **6**, e17100 (2017).
5. Akahane, Y., Asano, T., Song, B.-S. & Noda, S. High- Q photonic nanocavity in a two-dimensional photonic crystal. *Nature* **425**, 944–947 (2003).

6. Asano, T., Ochi, Y., Takahashi, Y., Kishimoto, K. & Noda, S. Photonic crystal nanocavity with a Q factor exceeding eleven million. *Opt. Express* **25**, 1769–1777 (2017).
7. Nozaki, K. et al. Femtofarad optoelectronic integration demonstrating energy-saving signal conversion and nonlinear functions. *Nat. Photon.* **13**, 454–459 (2019).
8. Crosnier, G. et al. Hybrid indium phosphide-on-silicon nanolaser diode. *Nat. Photon.* **11**, 297–301 (2017).
9. Takahashi, Y. et al. A micrometre-scale Raman silicon laser with a microwatt threshold. *Nature* **498**, 470–474 (2013).
10. Nozaki, K. et al. Ultralow-power all-optical RAM based on nanocavities. *Nat. Photon.* **6**, 248–252 (2012).
11. Lodahl, P., Mahmoodian, S. & Stobbe, S. Interfacing single photons and single quantum dots with photonic nanostructures. *Rev. Mod. Phys.* **87**, 347–400 (2015).
12. Sun, S., Kim, H., Luo, Z., Solomon, G. S. & Waks, E. A single-photon switch and transistor enabled by a solid-state quantum memory. *Science* **361**, 57–60 (2018).
13. Morin, O., D'Auria, V., Fabre, C. & Laurat, J. High-fidelity single-photon source based on a type II optical parametric oscillator. *Opt. Lett.* **37**, 3738–3740 (2012).
14. Morin, O. et al. Remote creation of hybrid entanglement between particle-like and wave-like optical qubits. *Nat. Photon.* **8**, 570–574 (2014).
15. Inagaki, T. et al. Large-scale Ising spin network based on degenerate optical parametric oscillators. *Nat. Photon.* **10**, 415–419 (2016).
16. Kippenberg, T., Spillane, S. & Vahala, K. Kerr-nonlinearity optical parametric oscillation in an ultrahigh- Q toroid microcavity. *Phys. Rev. Lett.* **93**, 083904 (2004).
17. Grudinin, I. S. et al. Ultra high Q crystalline microcavities. *Opt. Commun.* **265**, 33–38 (2006).
18. Stern, B., Ji, X., Okawachi, Y., Gaeta, A. L. & Lipson, M. Battery-operated integrated frequency comb generator. *Nature* **562**, 401–406 (2018).
19. Shen, B. et al. Integrated turnkey soliton microcombs. *Nature* **582**, 365–369 (2020).
20. Kippenberg, T. J., Gaeta, A. L., Lipson, M. & Gorodetsky, M. L. Dissipative Kerr solitons in optical microresonators. *Science* **361**, eaan8083 (2018).
21. Lu, X. et al. Milliwatt-threshold visible–telecom optical parametric oscillation using silicon nanophotonics. *Optica* **6**, 1535–1541 (2019).
22. Sayson, N. L. B. et al. Octave-spanning tunable parametric oscillation in crystalline Kerr microresonators. *Nat. Photon.* **13**, 701–706 (2019).
23. Tang, Y., Gong, Z., Liu, X. & Tang, H. X. Widely separated optical Kerr parametric oscillation in AlN microrings. *Opt. Lett.* **45**, 1124–1127 (2020).
24. John, S. Strong localization of photons in certain disordered dielectric superlattices. *Phys. Rev. Lett.* **58**, 2486–2489 (1987).
25. Yablonovitch, E. Inhibited spontaneous emission in solid-state physics and electronics. *Phys. Rev. Lett.* **58**, 2059–2062 (1987).
26. Matsko, A. B., Savchenkov, A. A., Strekalov, D., Ilchenko, V. S. & Maleki, L. Optical hyperparametric oscillations in a whispering-gallery-mode resonator: threshold and phase diffusion. *Phys. Rev. A* **71**, 033804 (2005).
27. Conti, C., Di Falco, A. & Assanto, G. Optical parametric oscillations in isotropic photonic crystals. *Opt. Express* **12**, 823–828 (2004).
28. Ramirez, D. M. et al. Degenerate four-wave mixing in triply resonant Kerr cavities. *Phys. Rev. A* **83**, 033834 (2011).
29. Azzini, S. et al. Stimulated and spontaneous four-wave mixing in silicon-on-insulator coupled photonic wire nano-cavities. *Appl. Phys. Lett.* **103**, 031117 (2013).
30. Matsuda, N., Kuramochi, E., Takesue, H., Shimizu, K. & Notomi, M. Resonant photon pair generation in coupled silicon photonic crystal nanocavities. In *The European Conference on Lasers and Electro-Optics CK_8_4* (Optical Society of America, 2017).
31. Taguchi, Y., Takahashi, Y., Sato, Y., Asano, T. & Noda, S. Statistical studies of photonic heterostructure nanocavities with an average Q factor of three million. *Opt. Express* **19**, 11916 (2011).
32. Colman, P. et al. Temporal solitons and pulse compression in photonic crystal waveguides. *Nat. Photon.* **4**, 862–868 (2010).
33. Combrié, S., Lehoucq, G., Moille, G., Martin, A. & De Rossi, A. Comb of high- Q resonances in a compact photonic cavity. *Laser Photon. Rev.* **11**, 1700099 (2017).
34. Alpegiani, F., Andreani, L. C. & Gerace, D. Effective bichromatic potential for ultra-high Q -factor photonic crystal slab cavities. *Appl. Phys. Lett.* **107**, 261110 (2015).
35. Tran, Q. V., Combrié, S., Colman, P. & De Rossi, A. Photonic crystal membrane waveguides with low insertion losses. *Appl. Phys. Lett.* **95**, 061105 (2009).
36. Miller, S. A. et al. Tunable frequency combs based on dual microring resonators. *Opt. Express* **23**, 21527–21540 (2015).
37. Yüce, E. et al. Adaptive control of necklace states in a photonic crystal waveguide. *ACS Photon.* **5**, 3984–3988 (2018).
38. Zhang, Y. et al. Squeezed light from a nanophotonic molecule. Preprint at <https://arxiv.org/abs/2001.09474> (2020).
39. Chang, L. et al. Ultra-efficient frequency comb generation in AlGaAs-on-insulator microresonators. *Nat. Commun.* **11**, 1331 (2020).
40. Fürst, J. et al. Low-threshold optical parametric oscillations in a whispering gallery mode resonator. *Phys. Rev. Lett.* **105**, 263904 (2010).
41. Bruch, A. W., Liu, X., Surya, J. B., Zou, C.-L. & Tang, H. X. On-chip $\chi^{(2)}$ microring optical parametric oscillator. *Optica* **6**, 1361–1366 (2019).
42. Zhao, Y. et al. Near-degenerate quadrature-squeezed vacuum generation on a silicon-nitride chip. *Phys. Rev. Lett.* **124**, 193601 (2020).
43. Vernon, Z. et al. Scalable squeezed-light source for continuous-variable quantum sampling. *Phys. Rev. Appl.* **12**, 064024 (2019).
44. Dutt, A. et al. On-chip optical squeezing. *Phys. Rev. Appl.* **3**, 044005 (2015).
45. Okawachi, Y. et al. Demonstration of chip-based coupled degenerate optical parametric oscillators for realizing a nanophotonic spin-glass. *Nat. Commun.* **11**, 4119 (2020).
46. Matsko, A. B. Hyperparametric frequency noise eater. *Phys. Rev. A* **99**, 023843 (2019).
47. Lu, X. et al. Chip-integrated visible–telecom entangled photon pair source for quantum communication. *Nat. Phys.* **15**, 373–381 (2019).
48. Clementi, M., Barone, A., Fromherz, T., Gerace, D. & Galli, M. Selective tuning of optical modes in a silicon comb-like photonic crystal cavity. *Nanophotonics* **1**, 205–210 (2019).
49. Marty, G., Combrié, S., De Rossi, A. & Raineri, F. Hybrid InGaP nanobeam on silicon photonics for efficient four wave mixing. *APL Photon.* **4**, 120801 (2019).

Publisher's note Springer Nature remains neutral with regard to jurisdictional claims in published maps and institutional affiliations.

© The Author(s), under exclusive licence to Springer Nature Limited 2020

Methods

Fabrication. The cavities are suspended membranes made of InGaP lattice-matched to GaAs. The PhC is created using e-beam lithography, dry etch of the hard mask, inductively coupled plasma etching of the holes and wet etching of the underlying material substrate to release the membrane⁵⁰. The large electronic gap (1.89 eV) prevents two-photon absorption when operating in the telecom spectral band, while the residual absorption rate $\Gamma_{\text{abs}} = 2\pi \times 10$ MHz is very low⁵¹.

Optical measurements. Optical measurements have been performed on a temperature-stabilized sample holder position stage and the two-way optical access is provided by a microscope objective lensed fibre, actuated by a three-axis nanopositioner stage, and a circulator. A tunable laser source is connected to the sample through a variable attenuator and the output is directly fed to the optical spectrum analyser.

High-resolution optical measurements are performed using an optical homodyne technique. A continuously swept laser is used to scan a Michelson interferometer where the sample replaces one of the mirrors. The detected fringes carry information about the electric field, and therefore Fourier analysis can be used to extract both the phase and the amplitude of the reflectivity, perform advanced noise filtering and also deduce the impulse response of the device. Further details are in the supplementary information of ref. ³³. This system has some features that are convenient for our study. First, the spectral resolution is about 20 MHz although the scan is fast (less than 10 s over a spectral range spanning 8 THz), which is adequate for a high-Q resonator. Second, the sensitivity is very high, thus we can use a very weak probe (about 100 nW) to ensure a purely linear response and, finally, this allows continuous-wave pump-probe analysis, as the pump is not detected as it is detuned from the local oscillator.

References

50. Combr  , S., Tran, Q. V., De Rossi, A., Husko, C. & Colman, P. High quality GaInP nonlinear photonic crystals with minimized nonlinear absorption. *Appl. Phys. Lett.* **95**, 221108 (2009).
51. Ghorbel, I. et al. Optomechanical gigahertz oscillator made of a two photon absorption free piezoelectric III/V semiconductor. *APL Photon.* **4**, 116103 (2019).

Acknowledgements

We thank G. Lehouc, S. Xavier and O. Parillaud for contributing to the InGaP PhC technology, I. Ghorbel for assistance with the experiments, and G. Moille, C. de Angelis, T. Debuisschert, E. Lallier, A. Brignon and A. Martin for fruitful and insightful discussions. This work is supported by a public grant overseen by the French National Agency (ANR) as part of the 'Investissements d'Avenir' programme (Labex NanoSaclay reference ANR-10-LABX-0035). This work has also received funding from the European Union's Horizon 2020 Research and Innovation Programme under the European Research Council (ERC) project HYPNOTIC (grant agreement number 726420) and the Marie Skłodowska-Curie project MOCCA (grant agreement number 814147).

Author contributions

S.C. and G.M. equally contributed to the measurements. F.R. and S.C. developed the technology. A.D.R. and G.M. analysed the results, A.D.R. developed the theory. All the authors contributed to writing the manuscript.

Competing interests

The authors declare no competing interests.

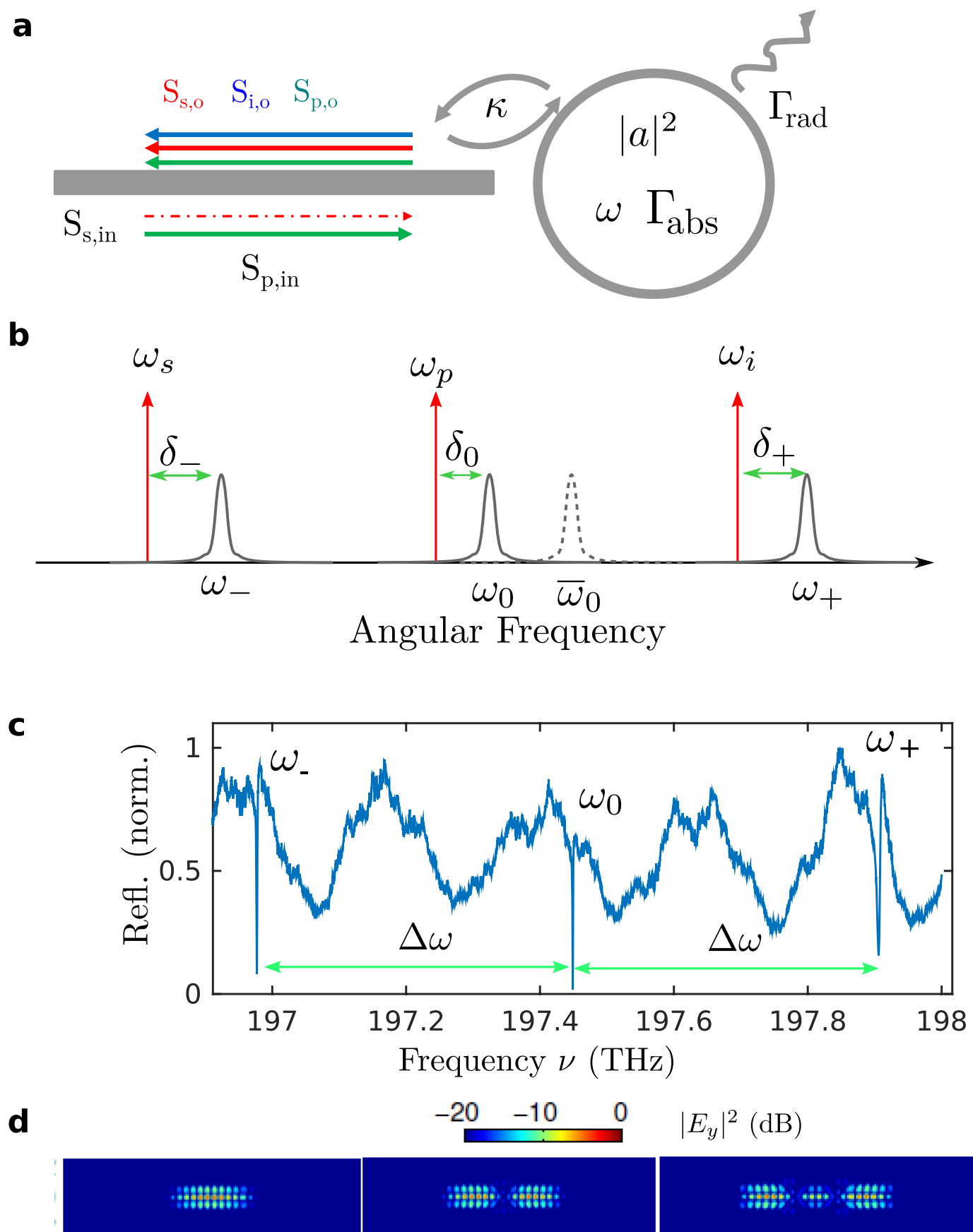
Additional information

Extended data is available for this paper at <https://doi.org/10.1038/s41566-020-00737-z>.

Supplementary information is available for this paper at <https://doi.org/10.1038/s41566-020-00737-z>.

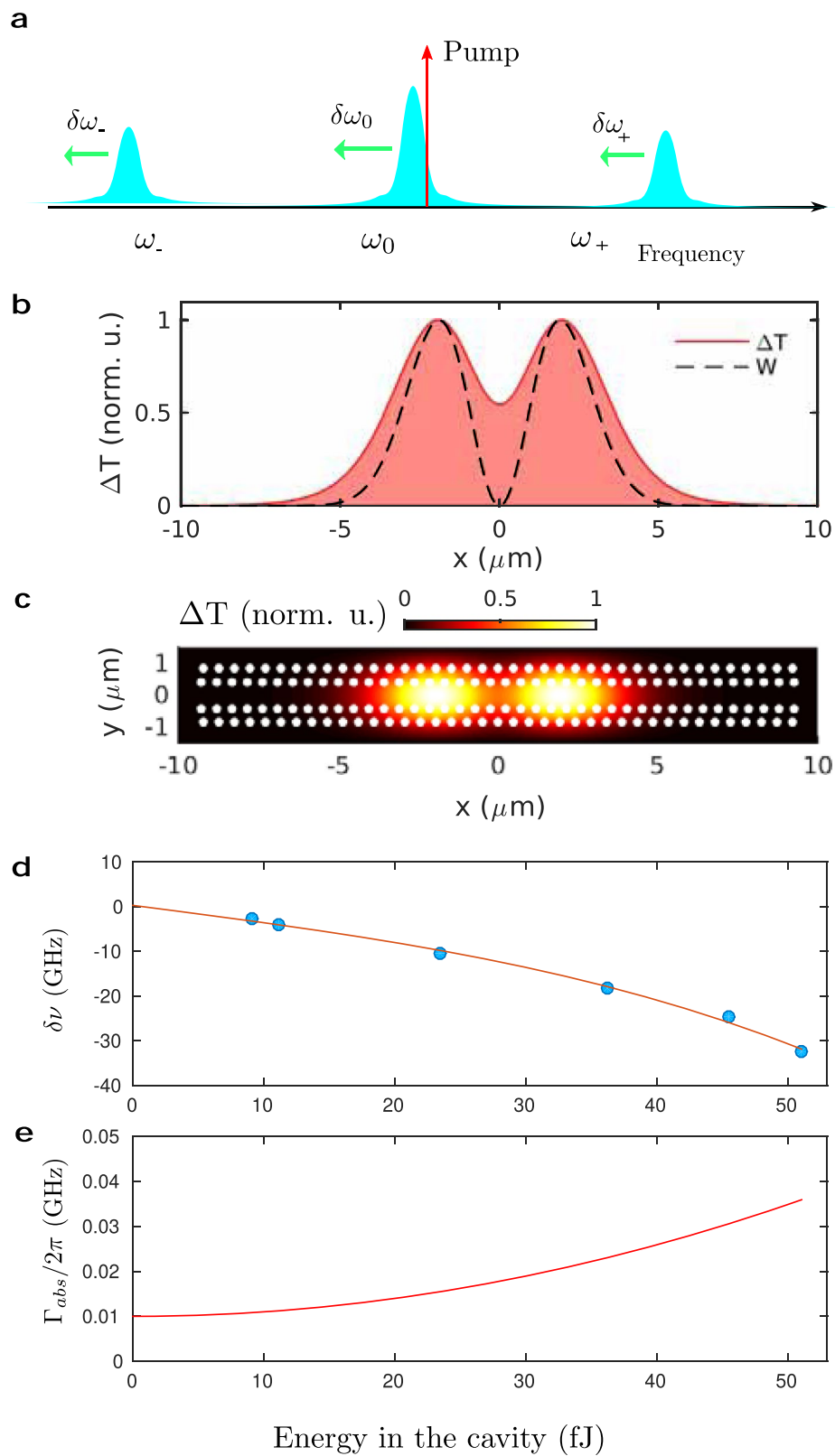
Correspondence and requests for materials should be addressed to A.D.R.

Reprints and permissions information is available at www.nature.com/reprints.

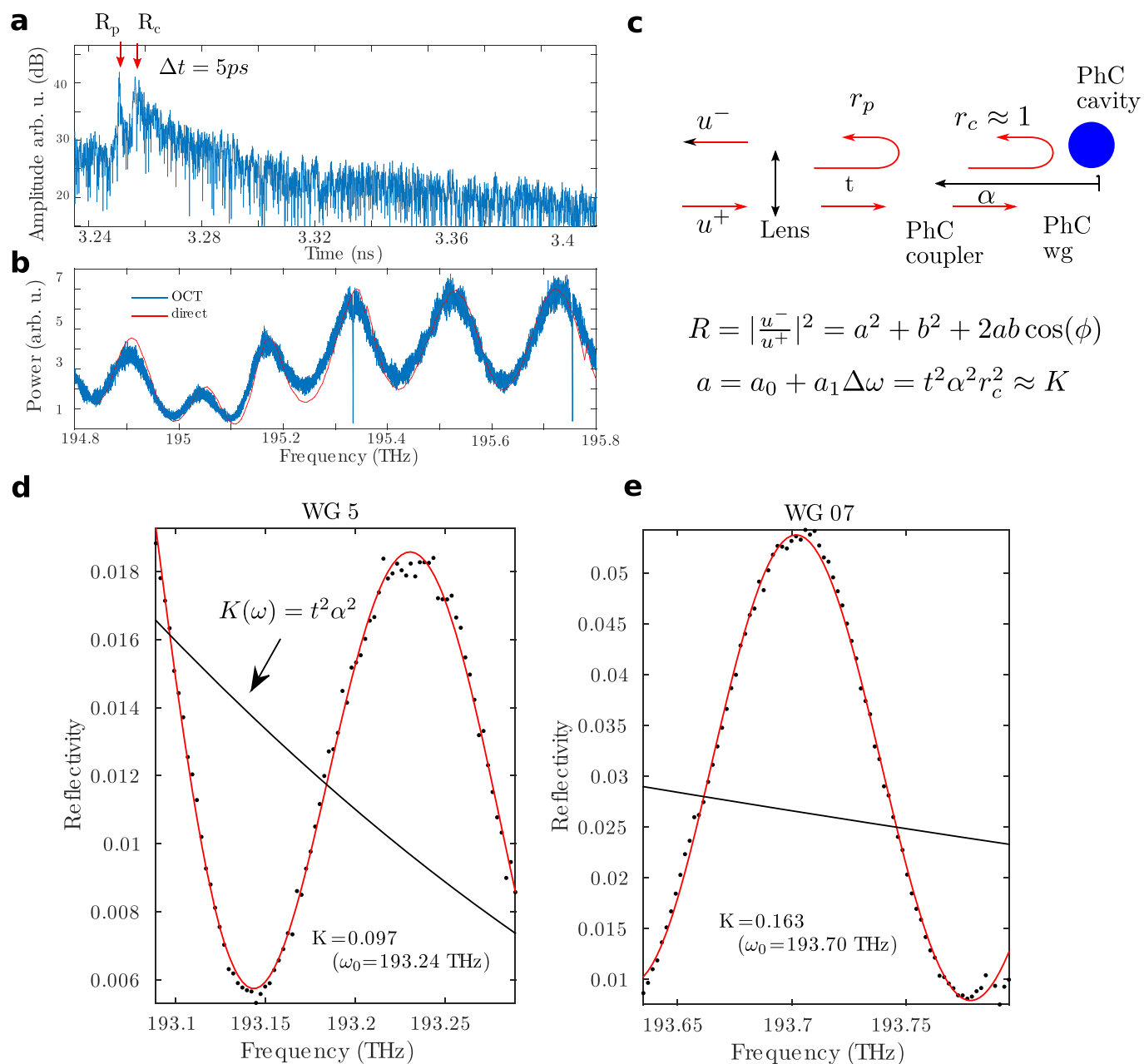


Extended Data Fig. 1 | See next page for caption.

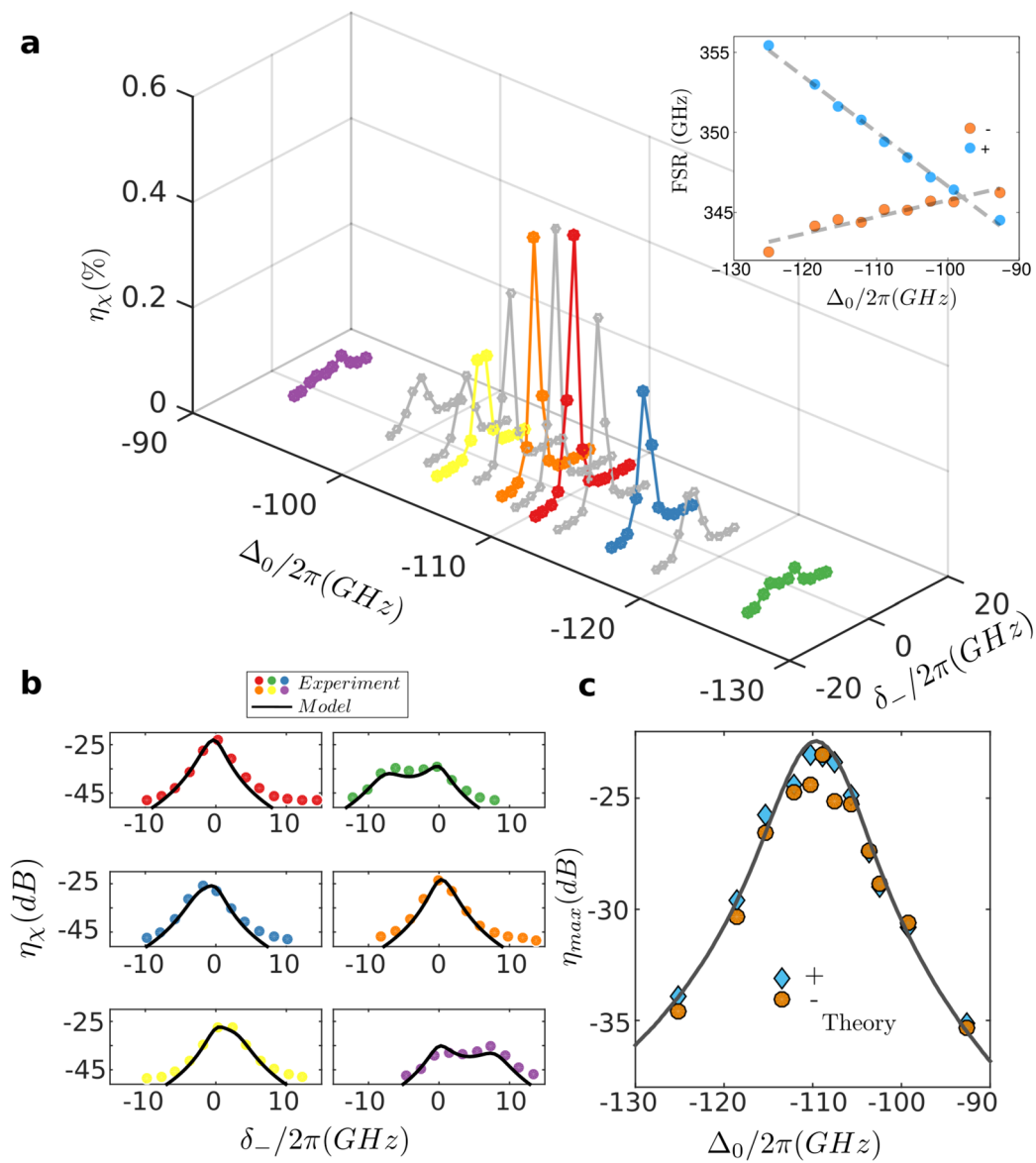
Extended Data Fig. 1 | Triply-resonant Cavity. **a:** Representation of a resonator coupled to a single- ended waveguide in the time-dependent coupled mode theory with definition of field in the waveguide s and in the cavity a , internal Γ abs and radiation loss Γ rad and waveguide coupling k ; **b** angular frequencies ω for the normal mode and excitation waves, 'cold' resonances ω and detuning δ . **c** Linear scattering spectrum measured using OCT revealing the $\omega \pm$ and ω_0 modes **d** and corresponding calculated modes.



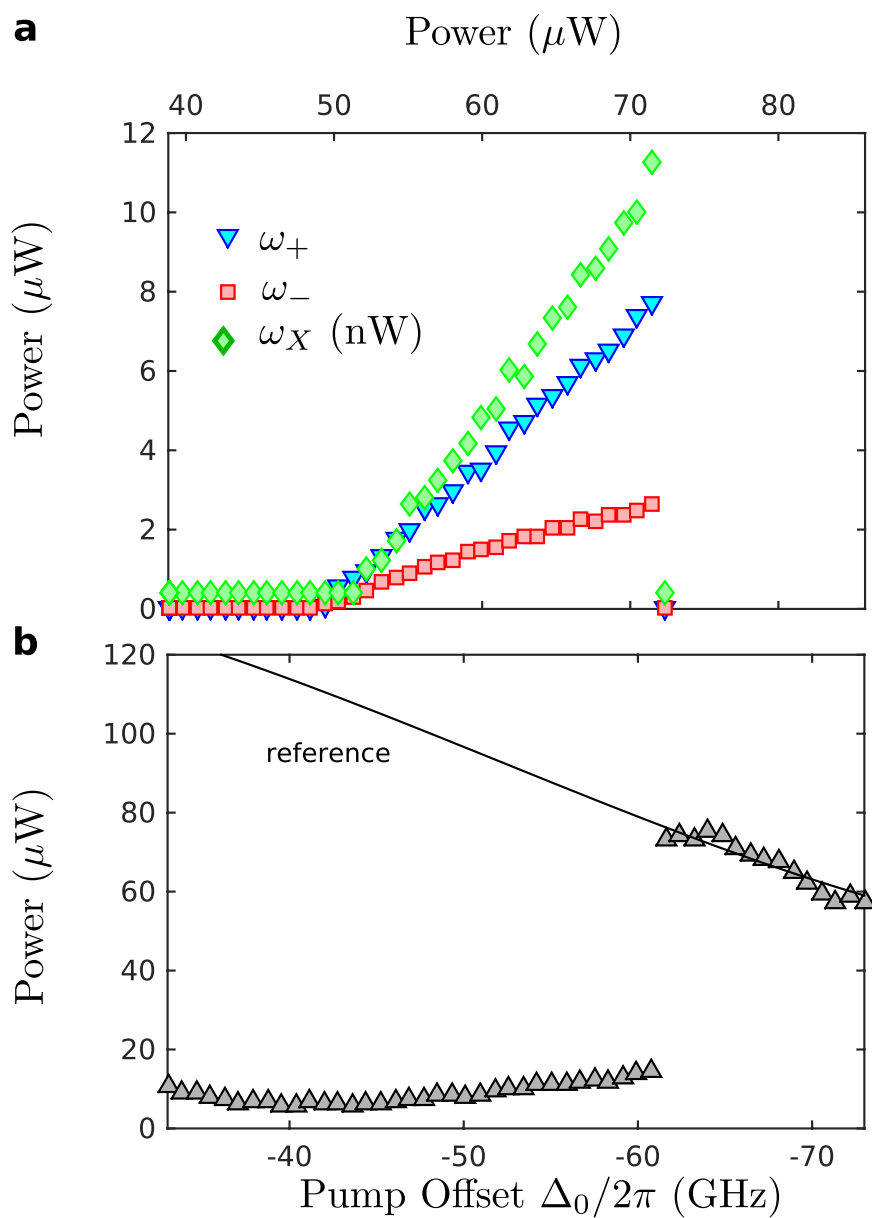
Extended Data Fig. 2 | Thermo-Optic Tuning. Description of the tuning measurement, with a pump pulling mode ω_0 and detecting all the resonances **a**; calculated profile of the temperature (solid filled) and the dissipated energy (dashed) **b** and corresponding 2D map **c**; measured spectral shift as a function of the energy stored in the mode (markers) and fit; **d** estimated absorption rate including nonlinear absorption **e**.



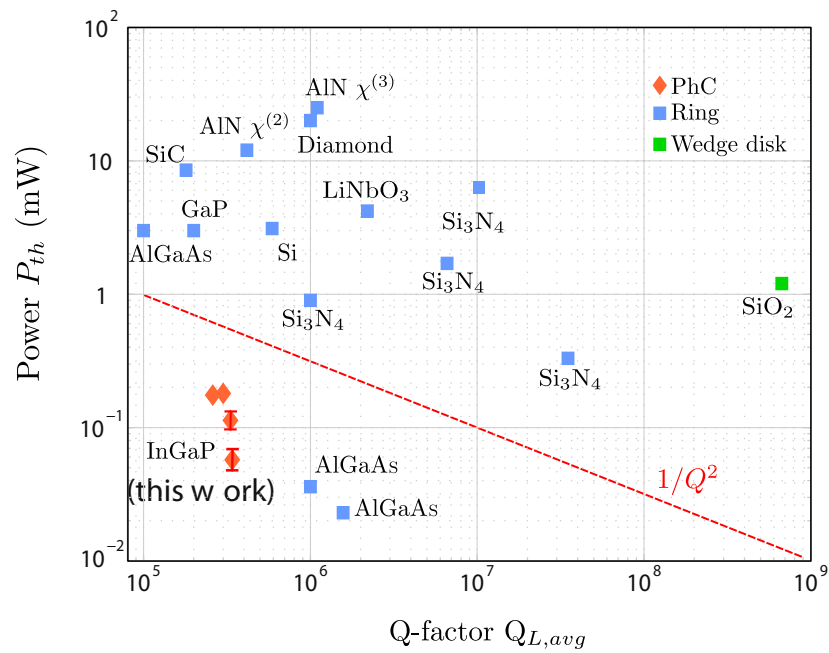
Extended Data Fig. 3 | Reflectivity Measurement and Model. Linear spectral characterization of a resonator using OCT. **a** Extracted temporal trace revealing a narrow peak (reflection from the end facet) and a broad dispersive peak (reflection from the cavity); **b** corresponding spectrum superimposed with the measurement of the reflection using a direct (non heterodyne) detection; **c** model representing reflection at the PhC coupler (=waveguide end facet) and from the cavity; **d** fitted reflection from cavity 5 and e cavity 7 from which the coupling factor K is extracted.



Extended Data Fig. 4 | Measured Stimulated FWM efficiency vs. Theory. Measurement of the stimulated FWM efficiency η_x as a function of the pump offset Δ_0 and probe detuning δ_- ; the corresponding measured FSR is in the inset **a**; comparison with the model (inset with colored frame); **b** $\max(\eta_x)$ as a function of the pump offset, experiment (symbols) and theory (solid line).



Extended Data Fig. 5 | Calibration of the OPO measurement. OPO measurement on cavity a5. **a** on-chip power in the sidebands as a function of the effective pump power P_{c0} (note that the idler ω_x is rescaled); **b** corresponding reflected pump power and calculated reflection when the pump is off- resonance (solid line), on chip pump power is 72 μ W. Same horizontal axis.



Extended Data Fig. 6 | OPO threshold. OPO pump threshold as a function of the Q factor compared with the state of the art in microring and racetrack resonators made of different materials. Details and references are in the Supplementary Table IV.